UC Irvine
UC Irvine Previously Published Works

Title
3-D X-Ray-Induced Acoustic Computed Tomography With a Spherical Array: A Simulation Study on Bone Imaging

Permalink
https://escholarship.org/uc/item/7bp2j4ts

Journal
IEEE Transactions on Ultrasonics Ferroelectrics and Frequency Control, 67(8)

ISSN
0885-3010

Authors
Li, Yang
Samant, Pratik
Wang, Siqi
et al.

Publication Date
2020-08-01

DOI
10.1109/tuffc.2020.2983732

Peer reviewed

eScholarship.org Powered by the California Digital Library
University of California

Author Manuscript

Author Manuscript

Author Manuscript

Author Manuscript

HHS Public Access

Author manuscript

IEEE Trans Ultrason Ferroelectr Freq Control. Author manuscript; available in PMC 2020 August 01.

Published in final edited form as:

IEEE Trans Ultrason Ferroelectr Freq Control. 2020 August ; 67(8): 1613–1619. doi:10.1109/TUFFC.2020.2983732.

3D X-ray-induced Acoustic Computed Tomography with a Spherical Array: A Simulation Study on Bone Imaging

Y. Li,

Shandong Key Laboratory of Medical Physics and Image Processing, Shandong Institute of Industrial Technology for Health Sciences and Precision Medicine, School of Physics and Electronics, Shandong Normal University, Jinan, Shandong 250358, China.

P. Samant,

The School of Biomedical Engineering at the University of Oklahoma, Norman, US

S. Wang,

The School of Electrical and Computer Engineering at the University of Oklahoma, Norman, US

A. Behrooz,

Alphabet, Inc.

D. Li*,

Shandong Key Laboratory of Medical Physics and Image Processing, Shandong Institute of Industrial Technology for Health Sciences and Precision Medicine, School of Physics and Electronics, Shandong Normal University, Jinan, Shandong 250358, China.

L. Xiang*

The School of Electrical and Computer Engineering at the University of Oklahoma, Norman, US

Abstract

X-ray-induced acoustic computed tomography (XACT) is a promising imaging modality combining high x-ray absorption contrast with the 3D propagation advantages provided by high resolution ultrasound waves. The purpose of this study was to optimize the configuration of a 3D XACT imaging system for bone imaging. A 280 ultrasonic sensors with peak frequency of 10 MHz was designed to distribute on a spherical surface to optimize the 3D volumetric imaging capability. We performed both theoretical calculations and simulations of this optimized XACT imaging configuration on a mouse-sized digital phantom containing various X-ray absorption coefficients. Iteration algorithm based on total variation has been used for 3D XACT image reconstruction. The spatial resolution of imaging was estimated to about 130 μm along both axial and lateral directions. We simulate XACT imaging of bone microstructures using digital phantoms generated from microCT images of real biological samples, showing XACT imaging can provide high resolution imaging of the mouse paw. Results of this study will greatly enhance the potential of XACT imaging in the evaluation of bone diseases for future clinical use.

Personal use is permitted, but republication/redistribution requires IEEE permission. See http://www.ieee.org/publications_standards/publications/rights/index.html for more information.

*(dengwang.li@139.com), (xianglzh@ou.edu).

Author Manuscript Author Manuscript Author Manuscript Author Manuscript

Keywords

X-ray-induced Acoustic Computed Tomography (XACT); X-ray absorption; 3D ultrasound array; 3D volumetric imaging; bone density map

I Itroduction

Bone's resistance to fracture depends on several factors, such as bone mass, microarchitecture, and tissue material properties [1]. The gold standard assessment of bone strength in clinic is performed by dual-energy x-ray absorptiometry (DEXA). It can measure bone mineral density (BMD) and trabecular bone score (TBS). Although it is considered the major predictor of bone strength, BMD only accounts for about 70% of fragility fractures. Moreover, BMD measured by DEXA imaging is limited by its two-dimensional nature, and it cannot capture the three-dimensional bone microarchitecture [2, 3]. An obvious pitfall of this method is that a larger bone will convey superior strength but may in fact have the same bone density as a smaller bone. Three-dimensional imaging modalities have held the potential to provide a much more comprehensive understanding of bone microarchitecture. State-of-the-art 3D bone imaging modalities, including magnetic resonance imaging (MRI) [4, 5], high resolution peripheral quantitative computed tomography (HR-pQCT) [6, 7], and modern multidetector row CT (MDCT) [8] have been investigated for quantitative assessment of bone microarchitecture at peripheral skeletal sites. Despite considerable success, these techniques suffer from slow scanning that causes motion artifacts [9], smaller field of view (FOV) susceptible to positioning error [10]; and, in the case of MRI, failure to provide quantitative BMD measures[8]. Micro-CT has achieved widespread use in the laboratory for imaging animal models with high imaging resolution. The application of Micro-CT to clinical research is limited to examine bone biopsy specimens because of its large radiation dose and invasiveness of the procedure [11]. Accurate measurement of these skeletal parameters through the development of better imaging technologies is critical to advancing fracture risk assessment and informing clinicians on the best treatment strategy.

In 2013, XACT imaging for biomedical purposes was first proposed and demonstrated and has since been investigated by different groups all over the world in various applications [12–18]. In XACT imaging, pulsed x-ray excitation of a sample results in localized heating (<mK), and subsequent thermoelastic expansion, this results in the emission of a detectable acoustic wave in the ultrasound regime, with an amplitude proportional to x-ray absorption. The conventional XACT imaging system utilizes a single ultrasound transducer and requires mechanical scanning for acquisition of a two-dimensional (2D) image, leading to tens of minutes of scanning [12, 19–21]. Recently, a new system [22], consisting of a sample that is irradiated by a nanosecond pulsed X-ray source, uses a ring array to capture the X-ray induced acoustic waves, and only single 2D slices of the sample can be obtained. In order to achieve 3D imaging capability, simulation is needed to design and optimize the new XACT imaging system before the prototype is being built.

In this paper, we use computer simulate to design and optimize the 3D XACT imaging system for volumetric bone imaging. Both theoretical calculation and simulations have been

Author Manuscript Author Manuscript Author Manuscript Author Manuscript

performed to optimize the ultrasound array detector configuration. *K*-wave simulation was used to simulate the X-ray induced acoustic signal generation, propagation, and attenuation in a digital phantom generated from micro-CT images. Then, iteration algorithm based on total variation has been used for 3D XACT image reconstruction and tested on three different simulation experiments.

II. Methods

A. Theory of XACT imaging

1) X-ray induced acoustic signal generation and detection—In XACT, we detect the acoustic signals generated by X-rays. When thermal confinement is satisfied, the physical models of XA signal generation and propagation for an arbitrary absorbing target can be written as [23],

$$\left(\nabla^2 - \frac{1}{\upsilon_s}\frac{\partial^2}{\partial t^2}\right)p\left(\overrightarrow{r},t\right) = -\frac{\beta}{C_p}\frac{\partial H\left(\overrightarrow{r},t\right)}{\partial t} \tag{1}$$

where $p\left(\overrightarrow{r},t\right)$ denotes the acoustic pressure rise at location $\overrightarrow{r}$ and time t, ν_s is the speed of sound, β denotes the thermal expansion coefficient, C_p denotes the specific heat capacity at a constant pressure, and $H\left(\overrightarrow{r},t\right)$ is the heating function. In the case of delta function excitation, the initial pressure rise p_0 related to X-ray absorption can be expressed by [23],

$$p_0 = \Gamma \cdot \eta_{th} \cdot \mu \cdot F \tag{2}$$

$\Gamma = \frac{\beta V_s^2}{C_p}$ is the Gruneisen absorbed energy that is converted to heat. η_{th} is the x-ray absorption coefficient, and F is the x-ray fluence with a unit of J/m^2. Since x-ray fluence attenuates exponentially when the photon propagation in the medium. Therefore, the X-ray fluence in distance r from the position of the X-ray source can be expressed as

$$F(r) = \frac{n \cdot E \cdot e}{A} e^{-\mu_A \rho r} \tag{3}$$

where n is the number of x-ray photons which set to 10^9 per pulse, μ_A is the mass-energy absorption coefficient, and E is the effective X-ray energy which is set to 20 KeV in the simulation [25, 26]. e is the electric charge with a value of $1.6 \times \frac{10^{-19} J}{eV}$. A is the radiation area of the X-ray beam. TABLE I lists all the parameters for bone [27]. Then equation (2) can be written as,

$$p_0 = \Gamma \eta_{th} \mu_a \frac{nEe}{A} \rho e^{-\mu_{en}\rho(r - r_0)} = M\rho(r) \tag{4}$$

where $p(r) = \rho e^{-\mu_a \rho(r - r_0)}$, r_0 represents the entrance position of X-ray beam, and $M = \Gamma \eta_{th} \mu_a \frac{nEe}{A}$ is a constant. Therefore, there is a linear relationship between initial pressure and bone density.

Author Manuscript Author Manuscript Author Manuscript Author Manuscript

B. Relationship between initial pressure and bone density

In our simulation study, we need to find out the relationship between initial pressure and the bone density matrix. The workflow is outlined below:

a. Micro-CT DICOM images from nu/nu adult mice were obtained [28], and 30×30×20 voxels from the mouse's paw as the region of interest (ROI) were selected and segmented using a threshold-based approach.

b. The HU values of the DICOM images can be extracted using the formula

$$\mathrm{HU} = pixel \times slope + Intercept \tag{5}$$

where the values of slope and intercept were 1 and −731, respectively, which can be found from the Micro-CT DICOM data.

c. The true density of the mouse bone is calculated based on the principle of the built-in module. Fat and muscle with fixed CT values were selected from the mice as calibrators. Through a large number of clinical trials and physical tests, the CT value of pure fat was −106.26, and the CT value of pure muscle was 31.74 [29]. The CT value of the corrected bone can be obtained by the formula,

$$CT = A \times HU + B \tag{6}$$

where A and B are obtained from the CT and HU values of fat and muscle, which are 0.46 and −773.26, respectively. The density of fat and the density of muscle are 0.11 g/cm^3 and 1.09 g/cm^3, respectively. The linear relationship between bone mineral density and CT value can be expressed as [30],

$$BMD = a \times CT + b \tag{7}$$

The density and CT values of fat and muscle were taken into equation (7), and the values of a and b were calculated. Equation (7) can be written as formula

$$BMD = 0.0013 \times CT + 1.049 \tag{8}$$

The bone density distribution of mice can be calculated by Equation (8).

C. Design of spherically curved array transducer

To optimize 3D XACT imaging, we simulated a spherically curved array transducer to capture X-ray-induced acoustic signals. For 3D XACT imaging, the x-ray pulse irradiates the target from the top, and a 3D sphere transducer array is used to capture the XA signals generated by the x-ray (Fig. 1(a)). Figure 2(a) shows the arrangement of transducers on a spherically curved surface which consists of 280 elements, forming seven tracks of equal width at a peak frequency of 10 MHz with 60% bandwidth. A hole of 12.38 mm diameter in the center of the transducer array allows the delivery of cone beam X-rays to the targets. The transducer had a detection angle of 92 degrees and a spherical radius of curvature of 40 mm. The element size was roughly 3mm × 3 mm. The field of view of this design can be caculated as [31],

Author Manuscript Author Manuscript Author Manuscript Author Manuscript

$$\xi < \frac{R}{2d}\lambda \approx \frac{20}{3}\lambda \tag{9}$$

where ξ is distance from the center of the focal plane, λ is the acoustic wavelength in the medium of tissue or water, R is the focal length, and d is a pitch between adjacent elements. Therefore, the field of view of the ultrasound array is calculated in which −6-dB lateral and axial spacing as 2.4 and 3.9 mm respectively.

D. K-wave simulations

We use the MATLAB *K*-Wave toolbox [32] to simulate X-ray-induced ultrasonic wave generation, propagation and attenuation in the bone. To demonstrate the imaging capability, we designed three testing models. Model 1 is a module consisting of five spherical absorbers, each of which has a radius of 300 μm (Fig.3(b)). It has been placed at the following coordinates: (0, 0, 0); (0, −10, 0); (0, 10, 0); (−10, 0, 0); and (10, 0, 0). Model 2 is a complex neuron-like structure (Fig.3(a)). Model 3 is bone density map of the mouse paw described in section B. The k-wave simulation was run in 3-D.

E. 3D XACT image reconstruction algorithm

Considering only partial projection data is available with the 3D spherical array detectors in this design, we propose to use a variation regularized iterative method for XACT image reconstruction [33]. Briefly, the inverse problem to be solved is

$$f = Ap_0 + \epsilon \tag{10}$$

Where p_0 is the initial pressure distribution to be recovered, f is the measured acoustic pressure as a function of time, and ϵ is an additional measurement error. The linear operator A models both ultrasonic wave propagation in the tissue and the measurement process. Numerical models of wave propagation can be used within the variational image reconstruction framework to find a regularized least-squares solution of (10) by solving the optimization problem,

$$P_{rec} := argmin\left\{\frac{1}{2}\|A\,p_0 - f\|_2^2 + \lambda J(p_0)\right\} \tag{11}$$

Here, λ > 0 is a regularization parameter and $J(p_0)$ is a suitable regularization functional that aims to encode a *priori* knowledge about the true solution, p_0. Then, an iterative reconstruction method based on a variational model is performed as described in Refs [30]. The image is updated by calculating the residual of the reconstructed image and the residual of the actual signal and iterated to obtain the reconstructed image. In the process of iterative reconstruction, the image with the smallest variation is obtained by the gradient descent method.

Author Manuscript Author Manuscript Author Manuscript Author Manuscript

III. RESULTS

A. Imaging resolution test

In order to investigate how the orientation of the ultrasound transducer array will affect the achievable resolution and overall quality of the XACT images, we first tested the imaging resolution in 3D. A single 100-μm XA point source moves along the x-, y-, and z-axes and the FWHM of the point source has been measured at different locations in three dimensions (Fig. 3(a)). When the point source moves 0, 2, 4, and 6 mm away from the center of the array along the X-axial direction, the FWHMs are 123 μm, 132 μm, 170 μm, and 275 μm, respectively. When the point source moves 0, 2, 4, and 6 mm away from the center of the array along the Y-axial direction, the FWHMs are 125 μm, 132 μm, 170 μm, and 275 μm, respectively. When the point source moves away from the center of the array along the Z-axial direction by −2, 0, 2, 4, and 6 mm, the FWHMs are 350 μm, 130 μm, 500 μm, 950 μm, and 1300 μm, respectively. We conclude that spatial resolution of this XACT imaging system is in the range of 123 μm–130 μm.

B. XACT image reconstruction of model 1

In addition to the imaging resolution test, five spherical X-ray absorbers with radius of 300 μm in a region of interest (ROI) was designed to test the imaging capability. The absorbers were positioned at the following coordinates (in voxels): (0, 0, 0); (0, In order to demonstrate that our 3D XACT system can be used for bone density map in 3D, we have simulated XACT imaging on mouse paws −10, 0); (0, 10, 0); (−10, 0, 0); and (10, 0, 0) (Fig. 3(b)). Fig. 3(c) shows Initial pressure (left) and reconstructed image (middle) in the x-y plane and profile plot (right) along the blue dashed line from the reconstructed image. The FWHM of three balls from left to right in Fig. 3(b) are 570, 440 and 570 μm, respectively. And Fig. 3(d) shows the corresponding images in x-z plane. The FWHM of the ball along the z-axis direction (green dotted line) is 442μm. Therefore, the designed XACT system has the best imaging resolution when the target is closer to the center of the detector array.

C. XACT image reconstruction of model 2

In order to improve the image quality of XACT imaging, we compared time-reversal image reconstruction algorithm and iterative image reconstruction algorithm for a complex neuron like structure as shown in Fig. 4.

Fig. 4(a) shows the XA initial in x–y, x-z and y–z planes. Fig. 4(b) shows the reconstructed XACT images in the same x–y, x-z and y–z plane using time-reversal algorithm. Fig. 4(c) shows the reconstructed XACT images using an iterative algorithm converged with 25 iterations. The zoom-in images show that the image quality is better by using the iterative algorithm compared with the time-reversal image reconstruction algorithm.

Fig. 5(a)–(d) show reconstructed XACT images in x–y plane using iterative algorithm with 10, 15, 20, 25 iterations, respectively. Figure 5 shows that the reconstructed pressure value will become closer to the real pressure as the number of iterations increase. However, the computation time will also increase.

Author Manuscript Author Manuscript Author Manuscript Author Manuscript

D. 3D XACT image reconstruction of model 3

In order to demonstrate the 3D imaging capability of the designed the system, we have simulated XACT imaging on mouse paws.

In vivo micro-CT DICOM images from nu/nu adult mice were obtained from a GE eXplore scanner with scan settings of 100 kV and 50 mA. The voxel size of the microCT images is about 100 μm [28]. A region of interest (ROI) with 30×30×20 voxels have been selected from a mouse paw, and the images have been segmented by using a threshold-based approach. In this study, tissues with a HU value greater than 3000 were defined as mouse bone. The detailed simulation workflow is described in section B and illustrated in Fig.1(b). The initial pressure was calculated by equation (4) for each point $\vec{r}$ in 3D. Fig. 6(b) shows the reconstructed image in a section perpendicular to the x-y plane with 450 μm between each slide. Fig. 6(c) shows the reconstructed XACT image of the bone density distribution on the mouse paw in 3D.

Fig. 7 shows the 3D XACT images of the mouse paw in different angles. Fig. 7(a) shows the initial pressure of the bone density distribution on the mouse paw in different angles. Fig. 7 (b) shows the corresponding 3D XACT images of the bone microstructure. These simulations clearly demonstrate that XACT imaging can be used to visualize the bone microstructure in three dimensions.

IV. Discussions

A. Comparison between time reversal method and iterative algorithm based on total variation method

The time reversal algorithm is an efficient and popular tomographic image reconstruction method for XACT image reconstruction in the cases where the complete data set is available [22] which is similar in many photoacoustic/optoacoustic imaging settings [34–36]. However, XACT measurement data are often incomplete (limited detection view and sparse sampling) for future clinical application, which results in artefacts in the images reconstructed with time reversal algorithm. To address this challenge, we propose to improve time reversal algorithm based on a variation regularized iterative method for XACT image reconstruction. In scenarios with incomplete or sub-sampled data, numerical model of wave propagation was used within the variational image reconstruction framework to find a proximal gradient descent solution of equation (11) by solving the optimization problem. The results show that the iterative reconstruction algorithm can be applied to a set of incomplete data from a mouse paw (Fig. 6) and the image quality has been improved compared to the standard time reversal algorithm (Fig. 4). Currently it takes 1.5 hours to reconstruct a 3D XACT image on an Intel(R) Core(TM) i5–9300H CPU @ 2.4GHz desktop with a k-grid size of 300×300×300. The image reconstruction speed can be improved on GPU in the future study.

B. Relationships between imaging resolution and ultrasound detector configuration

The relationship between the axial and lateral resolution differs depending on the configuration of the ultrasound probe in XACT. The lateral resolution of XACT imaging

Author Manuscript Author Manuscript Author Manuscript Author Manuscript

using a commercial ultrasonic probe is much lower than the axial resolution, but it can be significantly improved in the case of an array probe with a large angle of aperture. In this simulation, an array of ultrasonic detectors was designed and would be beneficial for future prototype development, considering the following three factors:

1. a large solid angle of the aperture of the ultrasonic detector;
2. a wide bandwidth and high center frequency of the ultrasonic detector match the frequency of the XA signal;
3. The relatively low electrical impedance of the ultrasonic detector avoids impedance mismatch with the cable and preamplifier.

A spherical curved array sensor designed in this paper has a large angular aperture and densely arranged components to achieve high sensitivity. The size of the selected array elements is much larger than the wavelength can avoid a reduction in reception voltage and bandwidth due to cable capacitance in the future prototype. The spatial resolution is in the range of 123–130 μm along both axial and lateral directions in the designed imaging system. However, the field of view of the transducer is limited to 2.4 and 3.9 mm, respectively.

C. Relationship between bone density and generated XA signals

The XA signal is proportional to the density of the X-ray absorber, and therefore XACT imaging offers a potential method through which the bone density can be quantified in images. Areas of samples with higher density will in turn absorb more x-ray photons, and therefore produce strong X-ray signals. This means that, if desired, it is possible to achieve quantitative bone density measurement with XACT imaging if the heat defect, and Grüneisen coefficient are accurately determined and the transducer and amplification system is well defined and calibrated. This has important biomedical applications towards bone density mapping. However, quantitative imaging so far in XACT has not been achieved. The development of quantitative image reconstruction algorithms remains an important future goal.

D. Future applications

At present, DEXA is a two-dimensional X-ray based imaging modality recognized as the gold standard for BMD measurement. XACT imaging as alternative to DEXA has the potential to provide 3D volumetric imaging for bone microstructure information. New compact x-ray sources with much shorter pulse duration (down to femtosecond) based on laser driven Betatron and Compton radiation providing X-rays with high flux (10^9 photons/s), and tunable energy (tens of KeV to Mev) could be idea excitation sources for XACT imaging in the future study [37–39]. Moreover, combining with X-ray imaging and ultrasound imaging, triplex imaging can provide rich information in bone density, elasticity information for osteoporosis for future application[40]. Like the rise of photoacoustic imaging in 2003[41–43], the field of X-ray induced acoustic computed tomography has been exponentially growing for various applications after year 2013. We hope to demonstrate the potential of 3D XACT imaging in assessing bone disease for future clinical use.

Author Manuscript Author Manuscript Author Manuscript Author Manuscript

V. Conclusions

A simulation study was conducted in this paper to evaluate the configuration of a 3D XACT imaging system optimized for bone imaging. Ultrasonic array with 280 sensors at peak frequencies of 10 MHz were designed to be distributed over the sphere to optimize 3D volumetric imaging capabilities. Theoretical calculations and simulations have been performed on a mouse-sized model containing various X-ray absorption coefficients. An iterative algorithm based on total variation has been used for 3D XACT image reconstruction of bone microstructures on mouse models. The results of this study will greatly enhance the potential of XACT imaging for future clinical applications in assessing bone disease.

Acknowledgments

This work was funded by the National Natural Science Foundation of China (NO.61471226, NO.61741117 and NO.11747085), Natural Science Foundation of Shandong Province (NO. JQ201516, 2018GGX101018), and the Taishan scholar project of Shandong Province (NO. tsqn20161023) to support the Yang Li's visit of Dr. Liangzhong Xiang's lab in The University of Oklahoma. This work was also partially supported by National Institute of Health (R37CA240806), American Cancer Society (133697-RSG-19-110-01-CCE), and the Oklahoma Center for the Advancement of Science and Technology (HR19-131) to Dr. Liangzhong Xiang. The authors would like to acknowledge the support from Stephenson Cancer Center bridge fund, IBEST-OUHSC fund, and a grant from the Research Council of the University of Oklahoma Norman Campus as well. The authors would like to thank Stephen Canady and Jack Merrill for proofreading the manuscript.

References

[1]. Mirzaali MJ et al., "Determinants of bone damage: An ex-vivo study on porcine vertebrae," PLoS One, vol. 13, no. 8, p. e0202210, 2018. [PubMed: 30114229]

[2]. Ammann P and Rizzoli R, "Bone strength and its determinants," Osteoporos Int, vol. 14 Suppl 3, pp. S13–8, 2003. [PubMed: 12730800]

[3]. Bolotin HH, "DXA in vivo BMD methodology: an erroneous and misleading research and clinical gauge of bone mineral status, bone fragility, and bone remodelling," Bone, vol. 41, no. 1, pp. 138–54, 7 2007. [PubMed: 17481978]

[4]. Wehrli FW et al., "Role of magnetic resonance for assessing structure and function of trabecular bone," Top Magn Reson Imaging, vol. 13, no. 5, pp. 335–55, 10 2002. [PubMed: 12464746]

[5]. Chang G, Pakin SK, Schweitzer ME, Saha PK, and Regatte RR, "Adaptations in trabecular bone microarchitecture in Olympic athletes determined by 7T MRI," J Magn Reson Imaging, vol. 27, no. 5, pp. 1089–95, 5 2008. [PubMed: 18425824]

[6]. Burrows M, Liu D, and McKay H, "High-resolution peripheral QCT imaging of bone micro-structure in adolescents," Osteoporos Int, vol. 21, no. 3, pp. 515–20, 3 2010. [PubMed: 19322507]

[7]. Krug R, Burghardt AJ, Majumdar S, and Link TM, "High-resolution imaging techniques for the assessment of osteoporosis," Radiol Clin North Am, vol. 48, no. 3, pp. 601–21, 5 2010. [PubMed: 20609895]

[8]. Chen C et al., "Quantitative imaging of peripheral trabecular bone microarchitecture using MDCT," (in English), Medical Physics, vol. 45, no. 1, pp. 236–249, 1 2018. [PubMed: 29064579]

[9]. Boutroy S, Bouxsein ML, Munoz F, and Delmas PD, "In vivo assessment of trabecular bone microarchitecture by high-resolution peripheral quantitative computed tomography," J Clin Endocrinol Metab, vol. 90, no. 12, pp. 6508–15, 12 2005. [PubMed: 16189253]

[10]. Boyd SK, "Site-specific variation of bone micro-architecture in the distal radius and tibia," J Clin Densitom, vol. 11, no. 3, pp. 424–30, Jul-Sep 2008. [PubMed: 18280194]

Author Manuscript Author Manuscript Author Manuscript Author Manuscript

[11]. Burghardt AJ, Link TM, and Majumdar S, “High-resolution computed tomography for clinical imaging of bone microarchitecture,” Clin Orthop Relat Res, vol. 469, no. 8, pp. 2179–93, 8 2011. [PubMed: 21344275]

[12]. Hickling S, Lei H, Hobson M, Leger P, Wang X, and El Naqa I, “Experimental evaluation of x-ray acoustic computed tomography for radiotherapy dosimetry applications,” Med Phys, vol. 44, no. 2, pp. 608–617, 2 2017. [PubMed: 28121381]

[13]. Hickling SHM, El Naqa I, “Feasibility of X-Ray Acoustic Computed Tomography as a Tool for Noninvasive Volumetric In Vivo Dosimetry,” Int J Radiat Oncol, vol. 90, p. S843, 2014.

[14]. Sampaio DRT UJ, Carneiro AAO, Pavoni JF, Pavan TZ, Borges LF, “X-ray acoustic imaging for external beam radiation therapy dosimetry using a commercial ultrasound scanner,” 2015 IEEE International Ultrasonics Symposium Proceedings, 16 November 2015 2015.

[15]. Jeesu Kim E-YP, Jung Yuhan, Kim Byoung Chul, Kim Joong Hyun, Yi Chul-Young, In Kim Jung, and Kim Chulhong, “X-Ray Acoustic-Based Dosimetry Using a Focused Ultrasound Transducer and a Medical Linear Accelerator,” IEEE TRANSACTIONS ON RADIATION AND PLASMA MEDICAL SCIENCES, vol. 1, no. 6, 11 2017 2017.

[16]. Li Y et al., “X-Ray-Induced Acoustic Computed Tomography for Osteoporosis,” (in English), Medical Physics, vol. 46, no. 6, pp. E668–E669, 6 2019.

[17]. Wang J, Nomura Y, Shirato H, Xing L, and Peng H, “Feasibility of X-Ray-Induced Acoustic Computed Tomography for Breast Imaging by Monte Carlo Simulation,” (in English), Medical Physics, vol. 46, no. 6, pp. E426–E426, 6 2019.

[18]. Wang S, Samant P, Robertson E, Liu H, and Xiang L, “3D X-Ray-Induced Acoustic Computed Tomography (3D XACT),” (in English), Medical Physics, vol. 46, no. 6, pp. E299–E299, 6 2019.

[19]. Xiang L, Han B, Carpenter C, Pratx G, Kuang Y, and Xing L, “X-ray acoustic computed tomography with pulsed x-ray beam from a medical linear accelerator,” Med Phys, vol. 40, no. 1, p. 010701, 1 2013. [PubMed: 23298069]

[20]. Xiang L, Tang S, Ahmad M, and Xing L, “TH-AB-209–07: High Resolution X-Ray-Induced Acoustic Computed Tomography,” Medical Physics, vol. 43, no. 6Part44, pp. 3864–3865, 2016.

[21]. Lei H et al., “Toward in vivo dosimetry in external beam radiotherapy using x-ray acoustic computed tomography: A soft-tissue phantom study validation,” Med Phys, Jun 29 2018.

[22]. Tang S et al., “X-ray-induced acoustic computed tomography with an ultrasound transducer ring-array,” (in English), Applied Physics Letters, vol. 110, no. 10, 3 6 2017.

[23]. Wang LV, “Tutorial on Photoacoustic Microscopy and Computed Tomography,” IEEE Journal on Selected Topics in Quantum Electronics, vol. 14, no. 1, pp. 171–179, 2008.

[24]. Tang S, Yang K, Chen Y, and Xiang L, “X-ray Induced Acoustic Computed Tomography for 3D Breast Imaging: A Simulation Study,” Medical Physics, vol. 94, no. Web Server, pp. 1–15, 2018.

[25]. Tang SS, Yang K, Chen Y, and Xiang LZ, “X-ray-induced acoustic computed tomography for 3D breast imaging: A simulation study,” (in English), Medical Physics, vol. 45, no. 4, pp. 1662–1672, 4 2018. [PubMed: 29479717]

[26]. Tang SS, Ramseyer C, Samant P, and Xiang LZ, “X-ray-induced acoustic computed tomography of concrete infrastructure,” (in English), Applied Physics Letters, vol. 112, no. 6, 2 5 2018.

[27]. https://www.itis.ethz.ch/virtual-population/tissue-properties/downloads/.

[28]. Behrooz A, Kask P, Meganck J, and Kempner J, “Automated Quantitative Bone Analysis in In vivo X-ray Micro-computed Tomography (μCT),” IEEE Transactions on Medical Imaging, vol. PP, no. 99, pp. 1–1, 2017.

[29]. Goodenough DJ, Weaver KE, Costaridou H, Eerdmans H, and Huysmans P, “A new software correction approach to volume averaging artifacts in CT ☆,” Computerized Radiology Official Journal of the Computerized Tomography Society, vol. 10, no. 2, pp. 87–98, 1986. [PubMed: 3754803]

[30]. Seeman E, Duan Y, Fong C, and Edmonds J, “Fracture site-specific deficits in bone size and volumetric density in men with spine or hip fractures,” Journal of Bone & Mineral Research the Official Journal of the American Society for Bone & Mineral Research, vol. 16, no. 1, pp. 120–127, 2010.

Author Manuscript Author Manuscript Author Manuscript Author Manuscript

[31]. Shin-Ichiro U, “Focused ultrasound transducer for thermal treatment,” International Journal of Hyperthermia the Official Journal of European Society for Hyperthermic Oncology North American Hyperthermia Group, vol. 31, no. 2, pp. 216–21, 2015.

[32]. Treeby BE and Cox BT, “k-Wave: MATLAB toolbox for the simulation and reconstruction of photoacoustic wave fields,” Journal of biomedical optics, vol. 15, no. 2, p. 021314, 2010. [PubMed: 20459236]

[33]. Arridge SR, Betcke MM, Cox BT, Lucka F, and Treeby BE, “On the adjoint operator in photoacoustic tomography,” Inverse Problems, vol. 32, no. 11, p. 115012, 2016.

[34]. Wang X, Xu Y, Xu MS, Fry ES, and Wang LV, “Photoacoustic tomography of biological tissues with high cross-section resolution: reconstruction and experiment,” Medical Physics, vol. 29, no. 12, pp. 2799–2805, 2002. [PubMed: 12512713]

[35]. Rui M, Adrian T, Vasilis N, and Daniel R, “Multispectral optoacoustic tomography (MSOT) scanner for whole-body small animal imaging,” Optics Express, vol. 17, no. 24, pp. 21414–21426, 2009. [PubMed: 19997381]

[36]. Andreas B, Eva H, Daniel R, and Vasilis N, “Video rate optoacoustic tomography of mouse kidney perfusion,” Optics Letters, vol. 35, no. 14, pp. 2475–7, 2010. [PubMed: 20634868]

[37]. Tsai HE et al., “Compact tunable Compton x-ray source from laser-plasma accelerator and plasma mirror,” (in English), Physics of Plasmas, vol. 22, no. 2, 2 2015.

[38]. Huang TW et al., “Highly efficient laser-driven Compton gamma-ray source,” (in English), New Journal of Physics, vol. 21, 1 9 2019.

[39]. Lemos N et al., “X-ray sources using a picosecond laser driven plasma accelerator,” (in English), Physics of Plasmas, vol. 26, no. 8, 8 2019.

[40]. Liwei SW zhao Li yue, merrill john, arellano jesus, Trevisi Luis, li yizhou, Xiang Liangzhong, Qu Junle, “Triplex radiometric, photoacoustic and ultrasonic imaging based on single-pulse excitation,” Optics Letters, 2020.

[41]. Zhang W et al., “Real-time photoacoustic sensing for photo-mediated ultrasound therapy,” Optics letters, vol. 44, no. 16, pp. 4063–4066, 2019. [PubMed: 31415547]

[42]. Xiang L, Tang S, Ahmad M, and Xing L, “High Resolution X-ray-Induced Acoustic Tomography,” Sci Rep, vol. 6, p. 26118, 5 18 2016. [PubMed: 27189746]

[43]. Pun SH et al., “Monolithic Multiband CMUTs for Photoacoustic Computed Tomography WithIn VivoBiological Tissue Imaging,” IEEE transactions on ultrasonics, ferroelectrics, and frequency control, vol. 65, no. 3, pp. 465–475, 2018.

Author Manuscript Author Manuscript Author Manuscript Author Manuscript

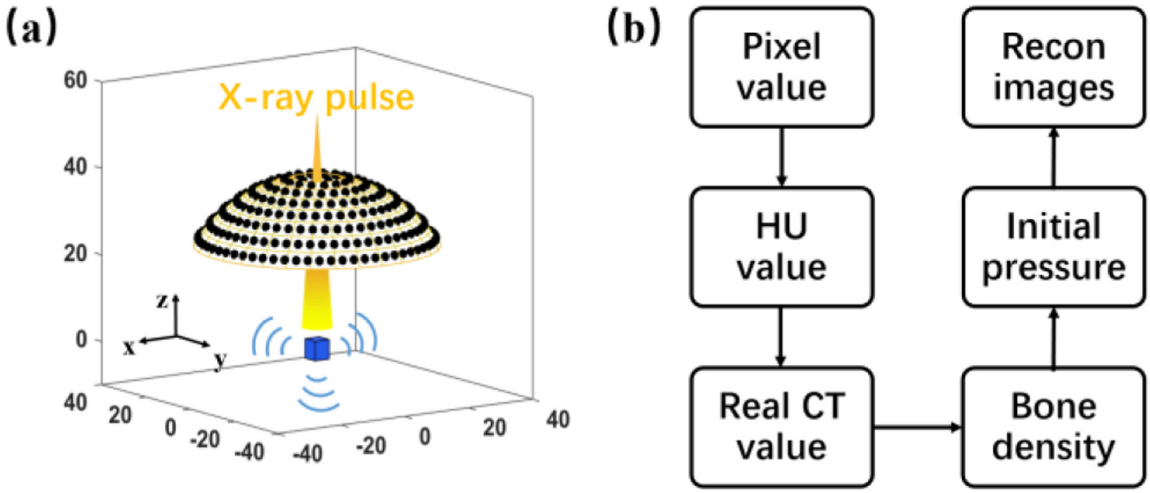

Fig. 1.

(a) Schematic diagram of X-ray induced acoustic signal generation and detection. (b) Simulation workflow of XACT on bone imaging.

Author Manuscript Author Manuscript Author Manuscript Author Manuscript

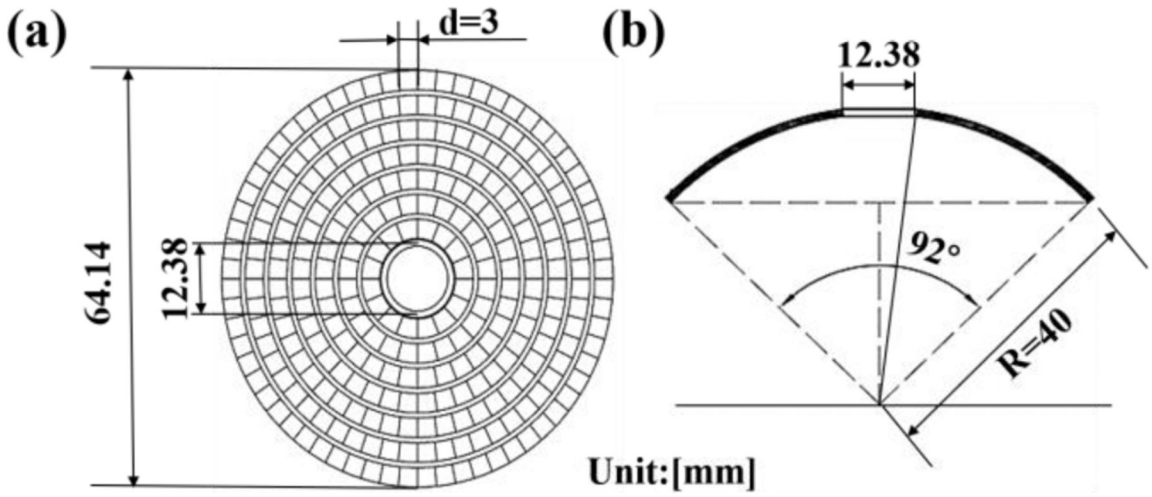

Fig. 2.

(a) Geometric arrangement of the spherical transducer array. (b) The front view of the array. The array had an opening angle of 92° and a spherical curvature radius of 40 mm.

Author Manuscript Author Manuscript Author Manuscript Author Manuscript

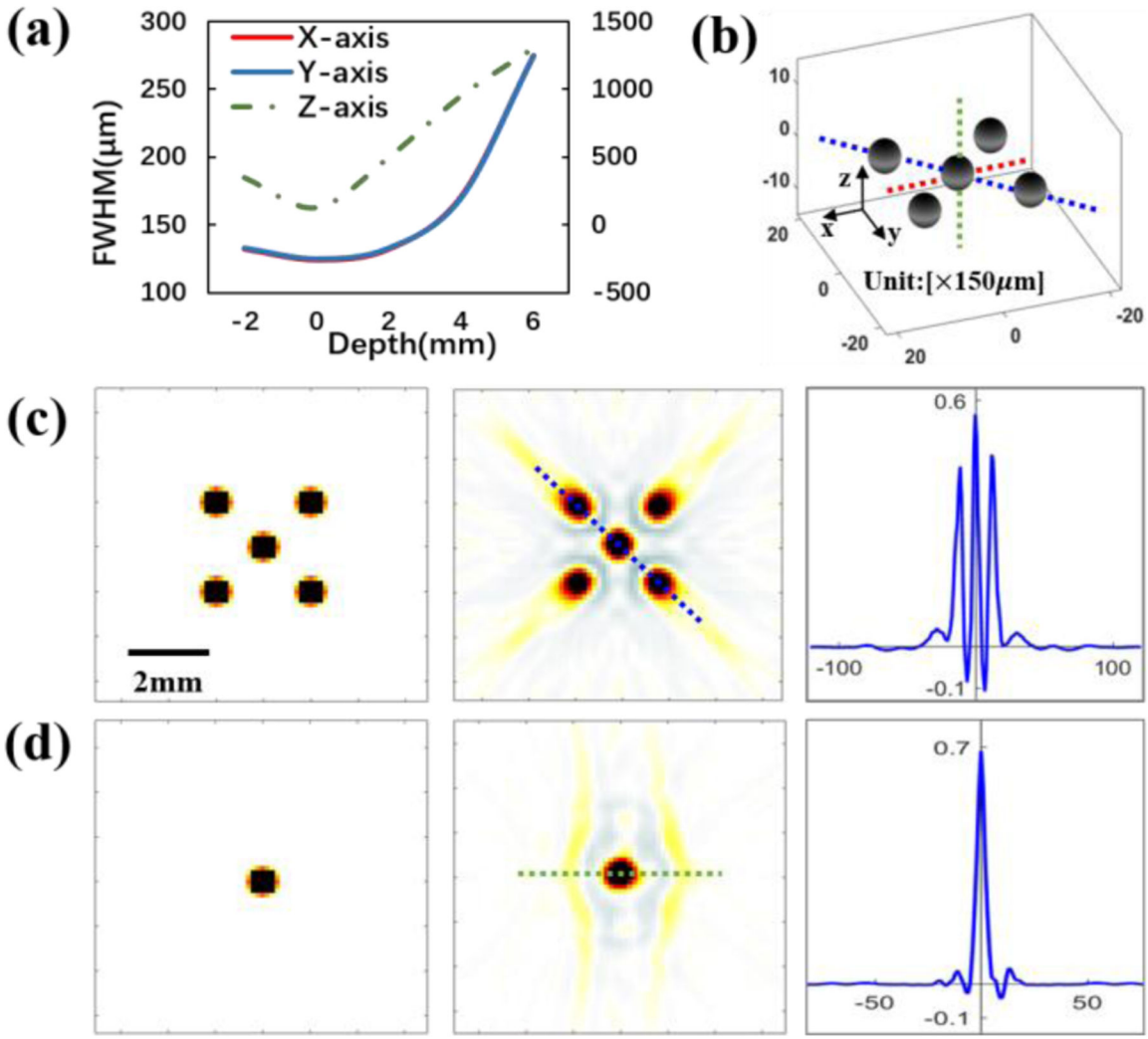

Fig. 3.

XACT images of model 1. (a) The FWHMs of the point spread function (PSF) varies with the depth in X-axial,Y-axial and Z-axial directions. (b) Sketch of five spherical absorbers. (c) Initial pressure (left) and reconstructed image (middle) in the x-y plane and profile plot (right) along the blue dashed line from the reconstructed image. (d) Initial pressure (left) and reconstructed image on the x-z plane (middle) and profile plot (right) along the green dashed line on the reconstructed image.

Author Manuscript Author Manuscript Author Manuscript Author Manuscript

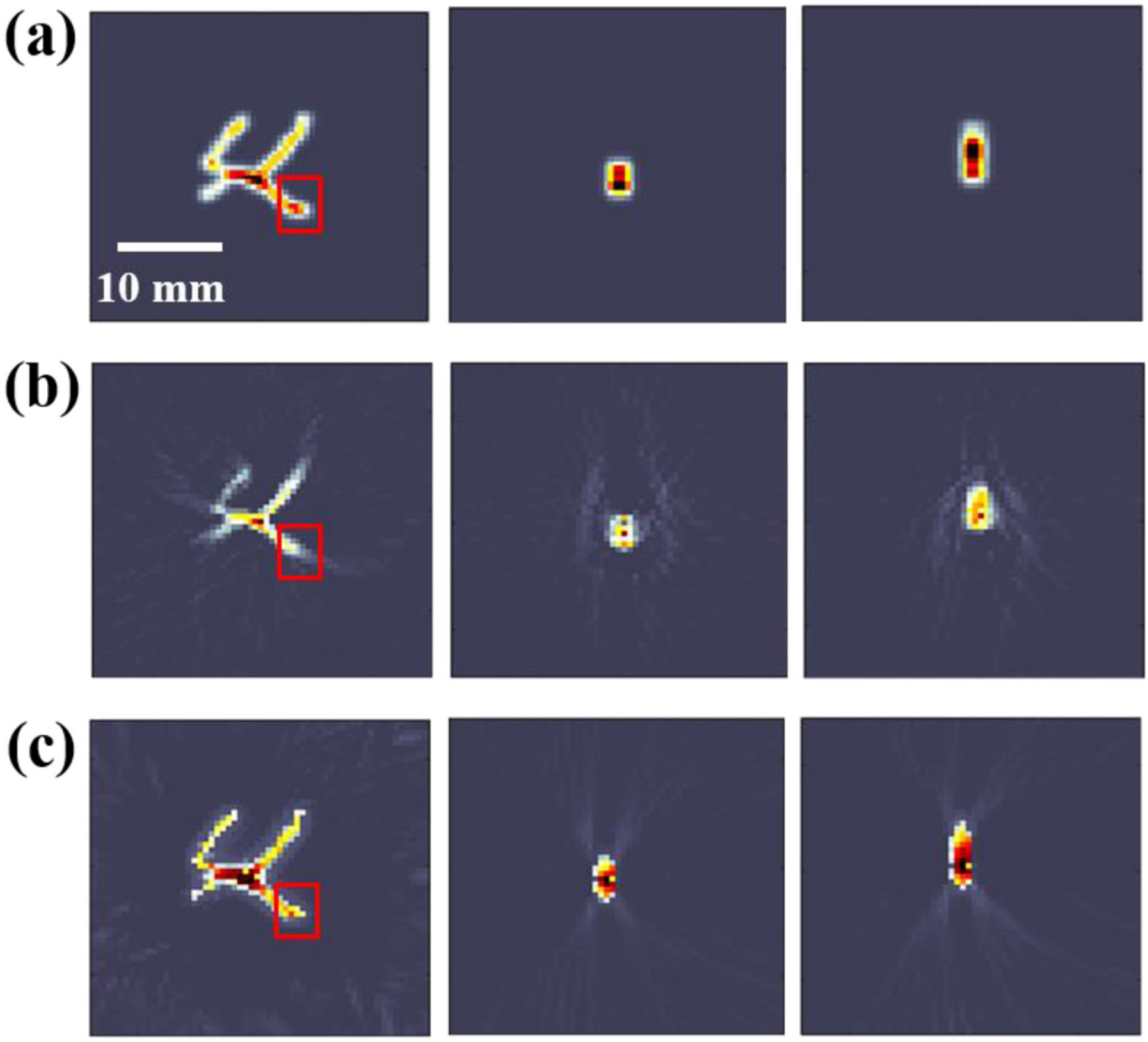

Fig. 4.

XACT images of model 2. (a) The initial pressure distribution in the x–y, x-z and y–z planes. (b) Reconstructed XACT image in the same x–y, x-z and y–z planes using time-reversal algorithm. (c) Reconstructed XACT image in the same x–y, x-z and y–z planes using an iterative algorithm based on gradient descent converged in 25 iterations.

Author Manuscript

Author Manuscript

Author Manuscript

Author Manuscript

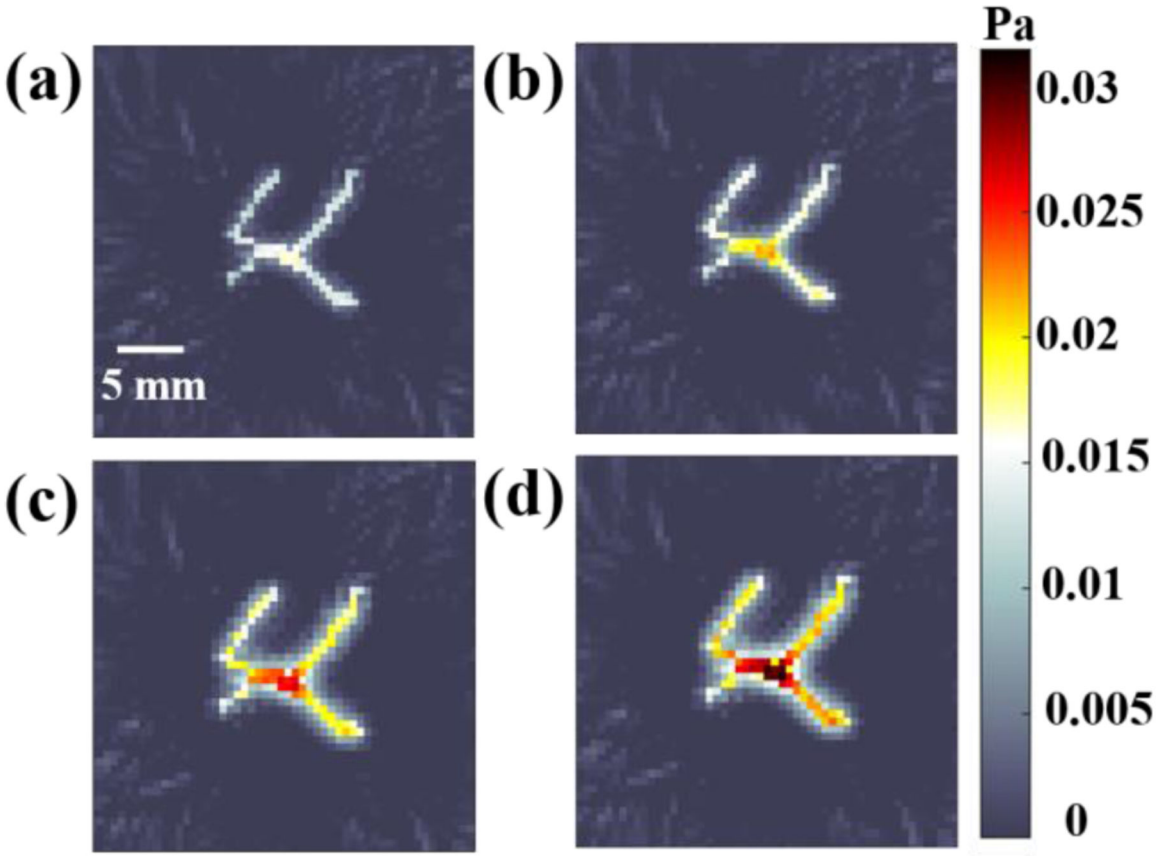

Fig. 5.

XACT images of model 2 with different iterations. (a)-(d) Reconstructed XACT image in x–y planes using an iterative algorithm in 10, 15, 20, 25 iterations, respectively. All XACT images used the same color bar.

Author Manuscript Author Manuscript Author Manuscript Author Manuscript

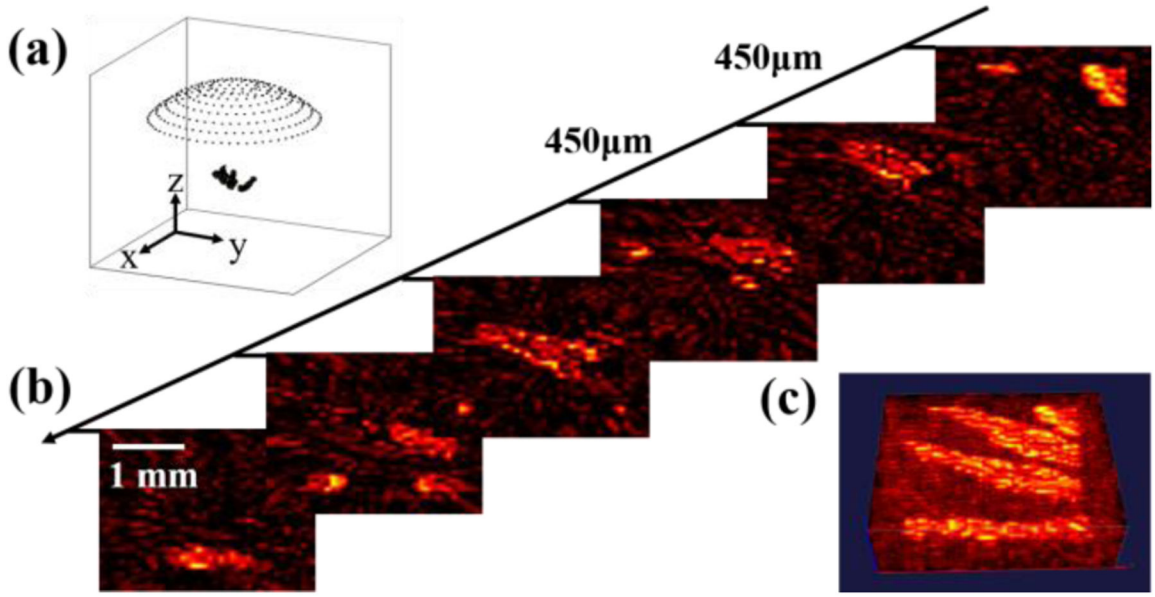

Fig. 6.

(a) The relative location of the ultrasound array and the imaging target. (b) The 2D reconstructed image slices extracted from a 3D image in the direction which is perpendicular to the x-y plane with 450μm between each 2D slices. (c) 3D XACT reconstructed image of the bone density distribution on a mouse paw.

Author Manuscript Author Manuscript Author Manuscript Author Manuscript

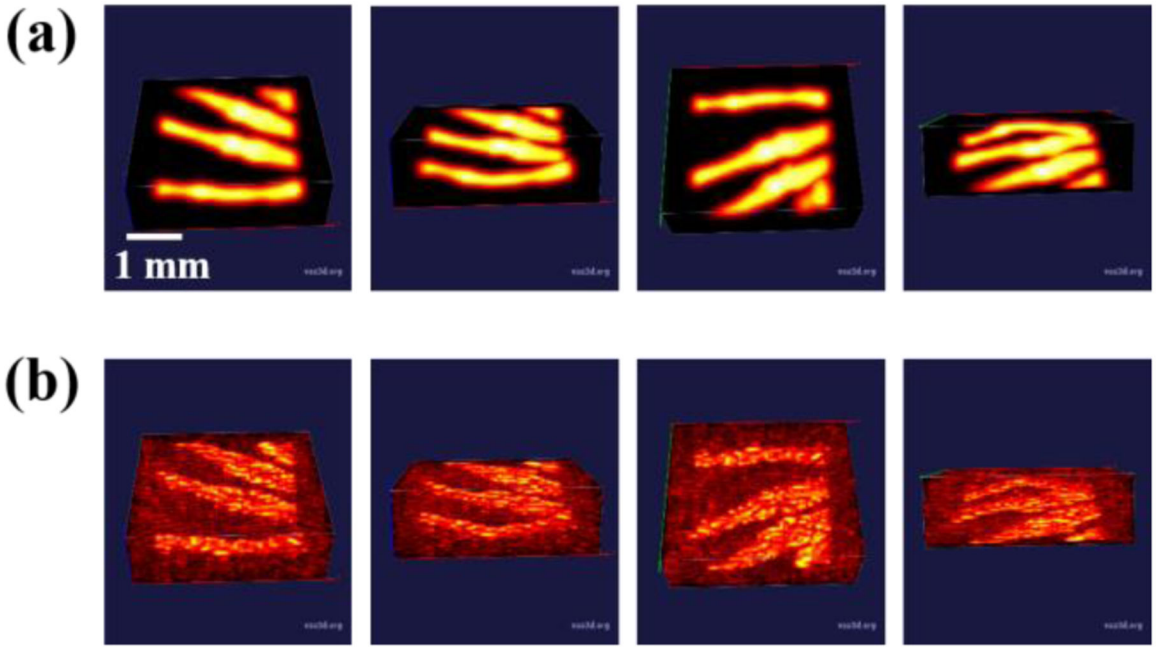

Fig. 7.

3D XACT images on paw in different angles. (a) 3D images of the initial pressure of the bone density distribution on the mouse paw. (b) 3D XACT reconstructed images of the bone density distribution on the mouse paw.

Author Manuscript

Author Manuscript

Author Manuscript

Author Manuscript

TABLE I

THERMAL ACOUSTIC PARAMETERS FOR THE BONE

Parameters	β **(×10^{-4}/K)**	v_s **(m/s)**	C_p **(J/kg·K)**	μ_a**@20KeV (cm^2/g)**
value	0.27	3515	1312.8	4